SOLIS

L. Evans, F. Fontani, C. Vastel, C. Ceccarelli, P. Caselli, A. López-Sepulcre, R. Neri, F. Alves, L. Chahine, C. Favre, et al.

A&A 657, A136 (2022)
https://doi.org/10.1051/0004-6361/202142147

Astronomy & Astrophysics

SOLIS

XIII. Nitrogen fractionation towards the protocluster OMC-2 FIR4★,★★

L. Evans[1,2], F. Fontani[2], C. Vastel[1], C. Ceccarelli[3], P. Caselli[4], A. López-Sepulcre[3,5], R. Neri[5], F. Alves[4], L. Chahine[5,6], C. Favre[3], and V. Lattanzi[4]

[1] IRAP, Université de Toulouse, 9 avenue du colonel Roche, 31028 Toulouse Cedex 4, France
e-mail: levans@irap.omp.eu
[2] INAF, Osservatorio Astrofisico di Arcetri, Largo E. Fermi 5, 50125 Firenze, Italy
[3] Univ. Grenoble Alpes, CNRS, Institut de Planetologie et d'Astrophysique de Grenoble (IPAG), 38000 Grenoble, France
[4] Max-Planck-Institut für extraterrestrische Physik (MPE), Giessenbachstrasse 1, 85748 Garching, Germany
[5] Institut de Radioastronomie Millimetrique (IRAM), 300 rue de la Piscine, Domaine Universitaire de Grenoble, 38406 Saint-Martin d'Hères, France
[6] Ecole doctorale de Physique, Université Grenoble Alpes, 110 rue de la Chimie, 38400 Saint-Martin-d'Hères, France

Received 3 September 2021 / Accepted 15 October 2021

ABSTRACT

Context. Isotopic fractionation is an important tool for investigating the chemical history of our Solar System. In particular, the isotopic fraction of nitrogen ($^{14}N/^{15}N$) is lower in comets and other pristine Solar System bodies with respect to the value measured for the protosolar nebula, suggesting a local chemical enrichment of ^{15}N during the formation of the Solar System. Therefore, interferometric studies of nitrogen fractionation in Solar System precursors are needed for us to obtain clues about our astrochemical origins.
Aims. In this work we have investigated the variation in the $^{14}N/^{15}N$ ratio in one of the closest analogues of the environment in which the Solar System was born: the protocluster OMC-2 FIR4. We present the first comparison at high angular resolution between HCN and N_2H^+ using interferometric data.
Methods. We analysed observations of the HCN isotopologues $H^{13}CN$ and $HC^{15}N$ in the OMC-2 FIR4 protocluster. Specifically, we observed the transitions $H^{13}CN$ (1−0) and $HC^{15}N$ (1−0) with the NOrthern Extended Millimeter Array (NOEMA) within the context of the IRAM Seeds Of Life In Space (SOLIS) Large Program. We combined our results with analysis of archival data obtained with the Atacama Large Millimeter Array of N_2H^+ and its ^{15}N isotopologues.
Results. Our results show a small regional variation in the $^{14}N/^{15}N$ ratio for HCN, from ∼250 to 500. The ratios in the central regions of FIR4, where the candidate protostars are located, are largely consistent with one another and within that range (∼300). They also show little variation from the part of the protocluster known to harbour a high cosmic-ray ionisation rate to the portion with a lower rate. We also found a small variation in the $^{14}N/^{15}N$ ratio of N_2H^+ across different regions, from ∼200 to ∼400.
Conclusions. These results suggest that local changes in the physical parameters occurring on the small linear scales probed by our observations in the protocluster do not seem to affect the $^{14}N/^{15}N$ ratio in either HCN or N_2H^+ and hence that this is independent of the molecule used. Moreover, the high level of irradiation due to cosmic rays does not affect the N fractionation either.

Key words. stars: formation – ISM: clouds – ISM: molecules

1. Introduction

The variety in the $^{14}N/^{15}N$ ratios found across the Solar System (SS) and beyond represents one of the biggest mysteries in astrochemistry. The $^{14}N/^{15}N$ ratio varies broadly among the objects of the SS itself, from approximately 140 in comets (Manfroid et al. 2009; Mumma & Charnley 2011; Shinnaka et al. 2014), to 50–300 in meteorites (Bonal et al. 2010; Aléon 2010), up to approximately 450 for the solar wind and Jupiter (Marty et al. 2011). This last value is believed to represent the protosolar nebula (PSN) value (Füri & Marty 2015), indicating that comets and other pristine SS small bodies are enriched in ^{15}N. However, the causes of this enrichment and, in particular, its relation to the chemical evolution of the PSN are not yet understood.

From the theoretical point of view, a former, popular explanation for the possible ^{15}N enrichment was the low temperature isotope exchange reactions (Terzieva & Herbst 2000; Rodgers & Charnley 2008), similar to those at the origin of molecular deuterium enrichment in cold dense cores (e.g. Ceccarelli et al. 2014a and references therein). However, recent chemical models have challenged this scenario due to the discovery of entrance barriers, which make these reactions unlikely to occur at low temperatures (Roueff et al. 2015; Wirström & Charnley 2018; Loison et al. 2019). The new models also rule out significant nitrogen fractionation processes in the most abundant molecules during the chemical evolution of a star-forming core. In fact, significant variations in nitrogen fractionation are theoretically predicted only in extragalactic environments strongly affected by very high fluxes of cosmic rays (Viti et al. 2019).

Those predictions are at odds with the large variations in $^{14}N/^{15}N$ measured in star-forming cores. In fact, the bulk $^{14}N/^{15}N$ ratio in the present-day local interstellar medium has been calculated to be approximately 300 (Romano et al. 2017;

★ NOEMA images are only available at the CDS via anonymous ftp to cdsarc.u-strasbg.fr (130.79.128.5) or via http://cdsarc.u-strasbg.fr/viz-bin/cat/J/A+A/657/A136
★★ SOLIS images will be provided by the Innovative Training Network (ITN) Astro-Chemical Origins (ACO) project as a deliverable.

Adande & Ziurys 2012; Colzi et al. 2018a), but large differences from the local interstellar value have been measured towards nearby pre- and proto-stellar objects, which seems to depend even on the molecule used (e.g. Womack et al. 1992; Bizzocchi et al. 2013; Hily-Blant et al. 2013, 2017, 2020; Daniel et al. 2013, 2016; Guzmán et al. 2017; Redaelli et al. 2018; De Simone et al. 2018). The spread in values becomes even larger when measured towards high-mass star-forming cores (e.g. Fontani et al. 2015; Zeng et al. 2017 and Colzi et al. 2018a,b). These are located in different parts of the Galaxy and hence, in principle, are associated with elementary $^{14}N/^{15}N$ ratios that are different from the local one due to the nitrogen isotopic galactocentric trend (Adande & Ziurys 2012; Colzi et al. 2018b) expected from nucleosynthesis models (Romano et al. 2017, 2019). However, the measured isotopic fractions cannot be explained only on the basis of the galactocentric trend (Colzi et al. 2018b; Fontani et al. 2021), indicating that local fractionation processes not yet included in the models may be at work.

Moreover, most of the observations performed so far have been obtained with single-dish telescopes, thus providing average values of the $^{14}N/^{15}N$ ratio over angular scales that can contain relevant variations in gas temperature and density. All this makes it challenging to identify whether the portions of the sources responsible for local enrichments (or depletions) in ^{15}N correspond to particular ranges of physical conditions (in particular, density, temperature and extinction).

In fact, the few follow-up observations performed at high angular resolution have suggested local gradients in the $^{14}N/^{15}N$ ratio. For example, Colzi et al. (2019) observed the high-mass protocluster IRAS 05358+3543 with a linear resolution of ∼0.05 pc, or ∼10 000 au, finding that the $^{14}N/^{15}N$ ratio in N_2H^+ shows an enhancement of a factor of ∼2 (from ∼100−220 to ≥200) going from the inner dense core region to the diffuse, parsec-scale envelope; these results were interpreted as being a consequence of selective photodissociation (Heays et al. 2014; Lee et al. 2021). This mechanism, which is due to the self-shielding of $^{14}N_2$, predicts an increase in the $^{14}N/^{15}N$ ratio in N_2H^+ in regions exposed to external UV irradiation, as indeed found by Colzi et al. (2019). This finding has been confirmed in a sample of infrared-dark cloud cores by Fontani et al. (2021), in which, again, the $^{14}N/^{15}N$ ratio measured from N_2H^+ increases in the external envelope of the dense cores.

Local changes in the $^{14}N/^{15}N$ ratio explainable by selective photodissociation have also been revealed in protoplanetary disks (Guzmán et al. 2017). In this case, the tracer used is HCN and a decrease in the $^{14}N/^{15}N$ ratio has been found in the external layers directly illuminated by the radiation field of the central star. This different behaviour between N_2H^+ and HCN with respect to selective photodissociation is expected since the ^{15}N-bearing species of N_2H^+ are formed from the molecular form of ^{15}N, $^{14}N^{15}N$ (dissociated at low extinctions), while those of HCN are formed from atomic ^{15}N (enhanced at low extinctions). Deviations from these predictions have been proposed by Furuya & Aikawa (2018), who claim the ^{15}N fractionation of N_2H^+ to be as low in the dense regions of pre-stellar cores as it is in the outer parts of the core, albeit for different reasons; in the dense regions it is because ^{15}N atoms are transformed into $^{15}NH_3$ on the surface of dust grains and lost to the gas phase, so fewer ^{15}N atoms will be available in the inner regions to form $N^{15}NH^+$ and $^{15}NNH^+$, while in outer parts this low fractionation is due to exposure to UV photons.

On the other hand, in very embedded, non-irradiated regions, the $^{14}N/^{15}N$ ratio should not change significantly, something that has been recently confirmed by observations with a linear resolution of ∼600 au (i.e. at core scales) obtained with the Atacama Large Millimeter Array (ALMA) of the protocluster OMC-2 FIR4, which have revealed negligible variations in the $^{14}N/^{15}N$ ratio in the embedded protocluster cores (Fontani et al. 2020). However, N_2H^+ is the only species investigated so far in $^{14}N/^{15}N$ at core scales, therefore more observational results are needed to shed light onto the ^{15}N fractionation process in cluster-forming environments.

In order to better investigate this, we obtained observations of isotopologues of HCN towards OMC-2 FIR4 in order to provide the first high angular resolution comparison of the $^{14}N/^{15}N$ ratio between HCN and N_2H^+ using interferometric data in one of the best analogues of the environment in which our SS was born. The $^{14}N/^{15}N$ ratio has already been investigated in our target at low angular resolution in multiple molecular species (Kahane et al. 2018). This work will prepare the observational ground for direct comparisons with both objects of the SS (in particular with pristine small bodies as proxies of the early SS) and with chemical models. In Sect. 2 we describe our target, the protocluster OMC-2 FIR4. The observations are presented in Sect. 3, the methods are described in Sect. 4 and the results are introduced in Sect. 5 and discussed further in Sect. 6. The main conclusions are given in Sect. 7.

2. Source background

OMC-2 FIR4 is a protocluster located in the Orion Molecular Cloud 2 (OMC-2), at a distance of approximately 393 ± 25 pc (Großschedl et al. 2018). The source consists of several continuum sources embedded in an extended, diffuse envelope (Shimajiri et al. 2008; López-Sepulcre et al. 2013; Kainulainen et al. 2017; Tobin et al. 2019; Neri et al., in prep.) and it is part of a long, pc-scale filament containing several young stellar objects (YSOs) and star-forming regions (e.g. Furlan et al. 2016; Hacar et al. 2018). There are two neighbouring far-infrared (FIR) sources: one to the south-east (FIR5), which is not included in our observations; and one to the north-west (FIR3), which is included in our observations. FIR3 itself is a Class I YSO (Tobin et al. 2019). The envelope of OMC-2 FIR4, having an angular size of ∼10−15″ or ∼4000–6000 au (e.g. Fontani et al. 2017; Fontani et al. 2020), is believed to have a temperature of 35–45 K and an average H_2 volume density of 1.2×10^6 cm^{-3} (Ceccarelli et al. 2014b), while FIR3, more compact (∼5″ or ∼2000 au), is believed to have a higher temperature because it is likely associated with a hot corino (Tobin et al. 2019; Ceccarelli et al., in prep.). OMC-2 FIR4 is believed to be one of the closest analogues to the early SS, due to its protocluster nature and evidence of external irradiation by an enhanced amount of energetic particles (Chaussidon et al. 2006; Ceccarelli et al. 2014b), probably accelerated by YSOs (Padovani et al. 2016). Increasing evidence has been found to suggest that the Sun was born in a similar protocluster environment (Adams 2010) that was subject to irradiation of a very similar dose of energetic particles (Gounelle et al. 2013; Ceccarelli et al. 2014b). As such, it is an important object to study as direct comparisons can be made with what we know of the early stages of our own SS in order to learn more about our astrochemical origins.

Multiple previous works studying OMC-2 FIR4 (Ceccarelli et al. 2014b; Fontani et al. 2017; Favre et al. 2018) have concluded with remarkable agreement that the cosmic-ray ionisation rate is enhanced in this source. In particular, Fontani et al. (2017) concluded from studying cyanopolyynes that a gradient in the cosmic-ray ionisation rate exists across the source, with the

eastern portion of the protocluster having an enhanced cosmic-ray ionisation rate of $\zeta \sim 10^{-14}$ s^{-1}. Moreover, that portion of the source seems to be more exposed to energetic phenomena such as outflows from FIR3 and the interior of FIR4 (e.g. Osorio et al. 2017; Lattanzi et al., in prep.).

3. Observations

Our observations were obtained using the IRAM NOrthern Extended Millimeter Array (NOEMA) Interferometer as part of the Seeds Of Life In Space (SOLIS) Large Program (Ceccarelli et al. 2017) with eight antennas on three days: April 29 and October 26, 2016 (both in C configuration) and January 16, 2017 (in A configuration). The phase centre was RA(J2000) = 05^{h}35^{m}26^{s}97, Dec(J2000) = –05°09′56″8 and the local standard of rest velocity was set to 11.4 km s^{-1}. Baselines range from 20 to 760 m, providing an angular resolution of ∼4.1 × 2.2″ (A+C configuration), corresponding to a linear scale of ∼860 au. The primary beam is ∼59.3″ at the representative frequency of 85 GHz. The system temperature, T_{sys}, was typically in between ∼60 and ∼100 K in all tracks and the amount of precipitable water vapour was generally ≤5 mm. The calibration of the bandpass and absolute flux scale was performed on 3C454.3 and MWC349 (∼1.05 Jy at 85.0 GHz), while 0524+034 and 0539–057 were used for calibration of the gains in phase and amplitude.

The lines were all observed with the Widex band correlator, providing a velocity resolution of 6.9 km s^{-1}. The continuum was imaged by averaging the line-free channels of the Widex and Narrow correlator units and subtracted from the spectrum in the (u,v)-domain. Calibration and imaging were performed using the CLIC and MAPPING softwares of the GILDAS[1] package using standard procedures. The continuum image was self-calibrated and the solutions were applied to the lines.

In order to estimate the amount of flux that is filtered out by the interferometer, we compare our spectra of HCN isotopologues to the single-dish spectra of the same lines; we used publicly available IRAM 30m observations of OMC-2 FIR4 to achieve this (Kahane et al. 2018). To this end, we extracted the HCN lines from the NOEMA cube within a polygon corresponding to the beam size of the single-dish observations (i.e. ∼28″); this was compared to the IRAM 30 m spectrum that had been resampled in velocity to match the resolution of our NOEMA observations (i.e. ∼6.9 km s^{-1}). The resulting comparison can be seen in Fig. 1 and showed that we recovered approximately 20% of the flux from both the H^{13}CN and HC^{15}N observations. As a result of the homogeneous effect of flux filtering on both lines, this caveat will have negligible impact on the calculated ^{14}N/^{15}N ratios, assuming that their distribution is similar. Moreover, this missing flux likely affects mostly the emission from the envelope rather than that from the dense cores, where the emission of H^{13}CN and HC^{15}N is concentrated, as we show later in this section.

For the purpose of comparison, we also utilised archival data consisting of N_2H^+ (1−0) emission along with emission of both of its ^{15}N isotopologues (^{15}NNH$^+$ (1−0) and N^{15}NH$^+$ (1−0)) towards OMC-2 FIR4 (ALMA project 2016.0.00681.S PI: F. Fontani). These lines were observed using ALMA in Band 3 (3 mm) with a velocity resolution of 0.2 km s^{-1} and a spatial resolution of about 600 au. Technical details of these observations

[1] The GILDAS software is developed at the IRAM and the Observatoire de Grenoble and is available at http://www.iram.fr/IRAMFR/GILDAS

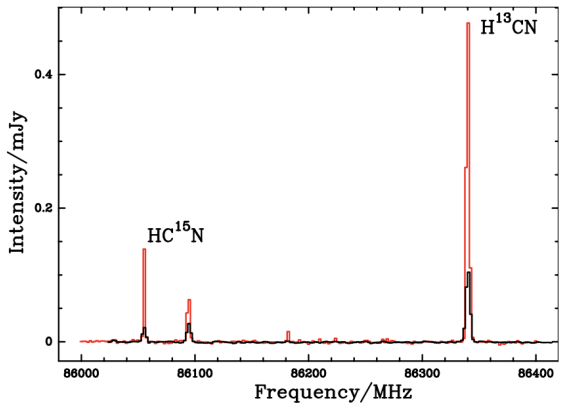

Fig. 1. Comparison between the flux recovered towards OMC-2 FIR4 by single-dish IRAM 30 m observations (red) and towards the region equivalent to the 30 m primary beam within the interferometric IRAM NOEMA observations of the same source (black). The figure shows that we recover approximately 20% of the flux in both the H^{13}CN line and the HC^{15}N lines. The line at 86.1GHz is SO (2_2−1_1).

(e.g. calibration, configurations used, weather conditions, sensitivity achieved) are given in Fontani et al. (2020). In the same way as for the HCN observations, the effect of flux filtering is the same for all isotopologues of N_2H^+, meaning that the effect on the ^{14}N/^{15}N ratios is minimal.

Table 1 shows the spectral parameters of the observed lines, including the parameters for the hyperfine (HF) components of N_2H^+ and its isotopologues. Figure 2 shows maps of the emission of both the H^{13}CN and HC^{15}N (1−0) lines averaged over the channels with signal-to-noise ratio (S/N) larger than 3, corresponding to an approximate velocity range of −1 to 18 km s^{-1} for H^{13}CN and 5 to 15 km s^{-1} for HC^{15}N. For comparison, Fig. 3 shows the continuum emission obtained from the NOEMA data at 3 mm published in Fontani et al. (2017). It can be seen from these maps that the H^{13}CN (1−0) emission is ubiquitously stronger than the HC^{15}N (1−0) emission across all regions of both FIR4 and FIR3. H^{13}CN and HC^{15}N show similar peak locations, with both having a peak in FIR3 and the north-western and north-eastern regions of the central part of FIR4. Three peaks in the southern inner region appear in HC^{15}N and are faintly seen in H^{13}CN among generally stronger surrounding emission. The most notable difference between the two maps is the presence of an eastern peak in the outer region of FIR4 in the H^{13}CN map while this is absent in the HC^{15}N map. It should also be noted that there is a hole in the H^{13}CN (and possibly HC^{15}N) emission towards the central region of FIR4 that is absent from the continuum emission and from any molecular line studied so far (e.g. Fontani et al. 2017, 2020; Favre et al. 2018).

The H^{13}CN (1−0) emission map suggests the presence of five gaseous cores in which the average emission is above 3σ rms (see Fig. 4). One is peaked on FIR3, the rest throughout FIR4. These sub-structures were chosen as the regions from which the spectra will be extracted and the isotopic ^{14}N/^{15}N ratio for HCN will be calculated.

As stated above, we extracted spectra of N_2H^+, ^{15}NNH$^+$ and N^{15}NH$^+$ (1−0), observed with ALMA, from the dataset published in Fontani et al. (2020). The analysis of these spectra will allow us to compare, for the first time at high angular resolution, the ^{14}N/^{15}N ratio simultaneously in HCN and N_2H^+ (i.e. the two molecules in which nitrogen fractionation should behave in an opposite way) if both are regulated by selective photodissociation. Figure A.1 shows the spectra that resulted from our

Table 1. Observational and spectral parameters of $H^{13}CN$ and $HC^{15}N$ as well as the HF components of N_2H^+ and its ^{15}N isotopologues.

Transition	Rest frequency GHz	Quantum numbers [(a)]	Statistical weight	E_u [K]	A_{ul} [s^{-1}]
$H^{13}CN$	86.3399214	1 → 0	9	4.14	2.23×10^{-5}
$HC^{15}N$	86.0549664	1 → 0	3	4.13	2.20×10^{-5}
$^{15}NNH^+$	90.2634867	1 1 → 0 1	3	4.33	3.30×10^{-5}
	90.2639119	1 2 → 0 1	5		
	90.2645041	1 0 → 0 1	1		
$N^{15}NH^+$	91.2042615	1 1 → 0 1	3	4.38	3.44×10^{-5}
	91.2059911	1 2 → 0 1	5		
	91.2085167	1 0 → 0 1	1		
N_2H^+	93.1716157	1 1 0 → 0 1 1	1	4.47	3.63×10^{-5}
	93.1719106	1 1 2 → 0 1 2	10		3.60×10^{-5}
	93.1720477	1 1 1 → 0 1 0	9		3.63×10^{-5}
	93.1734734	1 2 2 → 0 1 1	10		3.63×10^{-5}
	93.1737699	1 2 3 → 0 1 2	7		3.63×10^{-5}
	93.1739640	1 2 1 → 0 1 1	9		3.63×10^{-5}
	93.1762595	1 0 1 → 0 1 2	9		3.63×10^{-5}

Notes. All spectroscopic parameters have been taken from the CDMS (Endres et al. 2016). [(a)]The quantum numbers represent the J ($H^{13}CN$ and $HC^{15}CN$), J and F_1 ($^{15}NNH^+$ and $N^{15}NH^+$) and J, F_1 and F (N_2H^+) levels.

extraction from the chosen regions. In the case of FIR3, the spectrum shows no detection of N_2H^+ emission. This could be due to the destruction of this molecule by CO or it could be that the emission is so faint and extended that it has been resolved out by the interferometer. In the case of the ^{15}N isotopologues, $^{15}NNH^+$ also shows no emission towards FIR3, but there does appear to be a detection of $N^{15}NH^+$ as a clear peak is present in this spectrum. This suggests that the reason that the main N_2H^+ isotopologue is undetected is because the emission is resolved out by our interferometer as it is too extended; the presence of $N^{15}NH^+$ is explainable by the fact that this emission is likely to be more compact than the main isotopologue and so is not resolved out. For this reason, the $^{14}N/^{15}N$ ratio in FIR3 from N_2H^+ cannot be derived and will not be discussed further.

The N atom has a non-zero nuclear spin, which gives rise to hyperfine structure (HFS) splitting in spectra of N-bearing species, including HCN and N_2H^+, as well as the ^{15}N isotopologues of the latter. In the case of $H^{13}CN$ and $HC^{15}N$, the HFS is not resolved in our spectra due to the velocity resolution of these observations being insufficient to see the separate HFS components. However, in the spectra of N_2H^+ and its ^{15}N isotopologues, the velocity resolution is sufficient to resolve the HFS (see Fig. A.1). In the case of the ^{15}N isotopologues, we can resolve all three HF components, while in the case of the main isotopologue, we can observe seven HF components.

4. Methods

4.1. Extraction of the spectra and analysis

Using the MAPPING package of GILDAS (see Sect. 3), the spectra were extracted in flux density units (Jy) from the five regions illustrated in Fig. 4, which have been labelled depending on the position of the peak with respect to the phase centre, as: north-west (NW), north-east (NE), south (S), east (E) and FIR3. Due to the complexity of the emission and the partial overlap of some sub-structures, we decomposed the average emission map of $H^{13}CN$ by eye into the polygons shown in Fig. 4, which do not overlap and pick up the intensity peak of each sub-region. The CLASS package of GILDAS was employed to convert our spectra into temperature units (K) before they were imported into CASSIS[2].

As can be seen in Fig. A.1, the lines of $H^{13}CN$ and $HC^{15}N$ show generally a Gaussian shape; hence, each line was fitted with a single Gaussian in CASSIS using Levenberg-Marquardt (L-M) fitting. The fit provides several line parameters, among which is the full width at half maximum (FWHM), which was then used as one of the input parameters for local thermal equilibrium (LTE) analysis using CASSIS. In order to check our LTE assumption, which is satisfied if the H_2 density is larger than the critical density of the analysed transition, we computed the critical density of each of our lines from the equation:

$$n_{CRIT} = \frac{A_{ul}}{C_{ul}}. \quad (1)$$

In Eq (1), n_{CRIT} represents the critical density (cm^{-3}) while A_{ul} (s^{-1}) represents the Einstein coefficient and C_{ul} ($cm^{-3}\,s^{-1}$) represents the collisional coefficient. We use collisional coefficients taken from the CASSIS collision database and calculated by Hernandez-Vera et al. (2014) for HCN and by Daniel et al. (2005); Lique (2015) for N_2H^+. For the 1−0 transition we can assume that the ^{15}N isotopologues (and ^{13}C-isotopologues) have the same collisional coefficients as their respective main isotopologues. The critical density at 40 K was calculated to be 1.62×10^6 cm^{-3} for $H^{13}CN$, 1.59×10^6 cm^{-3} for $HC^{15}N$, 1.61×10^5 cm^{-3} for $^{15}NNH^+$, 1.66×10^5 cm^{-3} for $N^{15}NH^+$ and

[2] Based on analysis carried out with the CASSIS software (Vastel et al. 2015) and JPL (http://spec.jpl.nasa.gov/) and CDMS (https://cdms.astro.uni-koeln.de/classic/) molecular databases. CASSIS has been developed by IRAP-UPS/CNRS (http://cassis.irap.omp.eu).

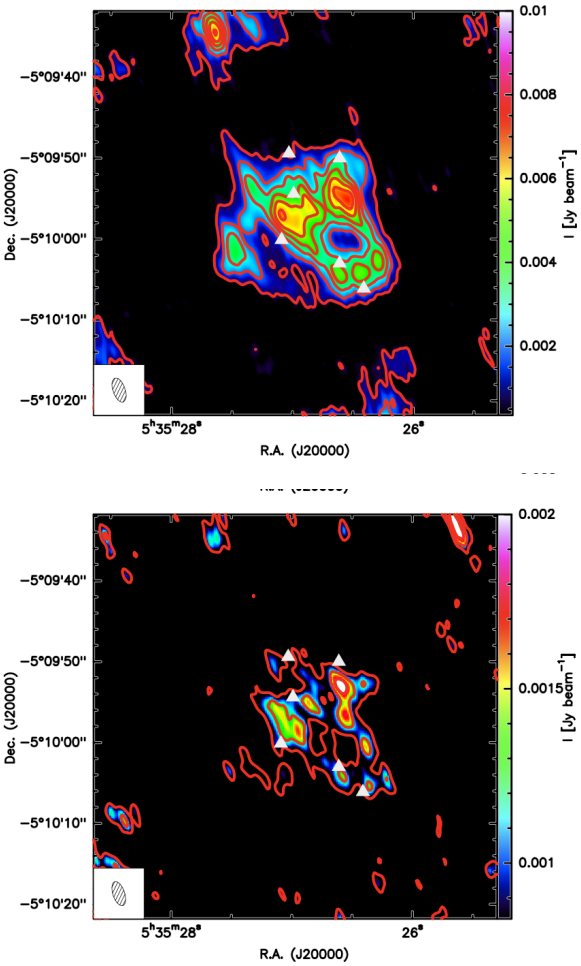

Fig. 2. *Upper panel*: $H^{13}CN$ (1−0) average emission map in colour scale and red contours. Contours start at the level of 4σ, corresponding to 0.70 mJy beam^{-1} (1σ = 0.18 mJy beam^{-1}) and are in intervals of 6σ, corresponding to 1.17 mJy beam^{-1}. *Lower panel*: $HC^{15}N$ (1−0) average emission map in colour scale and red contours. Contours start at the level of 4σ, corresponding to 0.84 mJy beam^{-1} (1σ = 0.21 mJy beam^{-1}) and are in levels of 4σ, corresponding to 0.84 mJy beam^{-1}. Continuum sources identified by Neri et al. (in prep.) are marked by white triangles. The wedge on the right indicates the range of flux density (Jy beam^{-1}). The ellipse in the bottom-left corner of each panel represents the NOEMA synthesised beam.

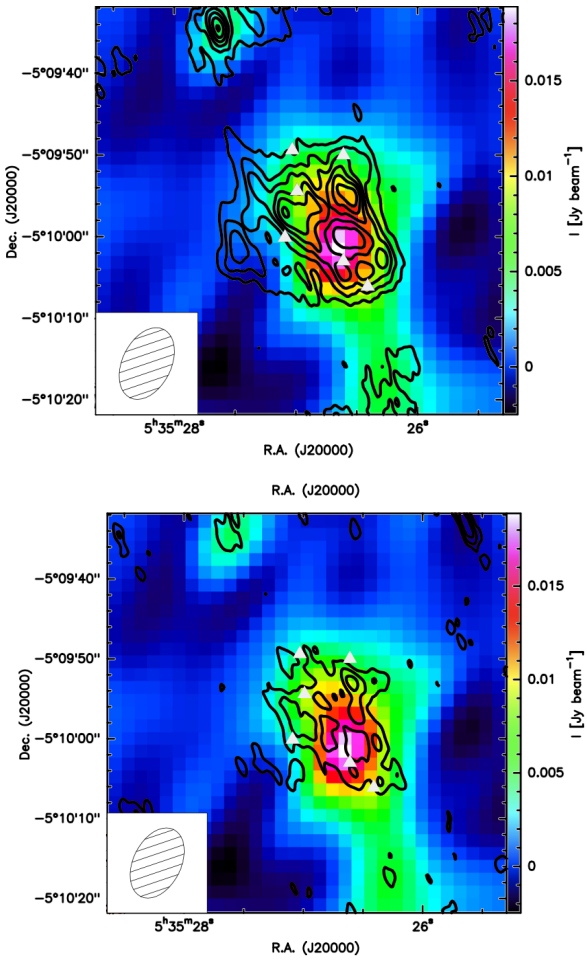

Fig. 3. *Upper panel*: continuum emission map at 3 mm (from Fontani et al. 2017) in colour scale with $H^{13}CN$ (1−0) emission overlaid in black contours. Contours start at the level of 4σ, corresponding to 0.70 mJy beam^{-1} (1σ = 0.18 mJy beam^{-1}) and are in intervals of 6σ, corresponding to 1.17 mJy beam^{-1}. *Lower panel*: same as the upper panel but the black contours show the $HC^{15}N$ (1−0) average emission. Contours start at the level of 4σ, corresponding to 0.84 mJy beam^{-1} (1σ = 0.21 mJy beam^{-1}) and are in levels of 4σ, corresponding to 0.84 mJy beam^{-1}. Continuum sources identified by Neri et al. (in prep.) are marked by white triangles. The wedge on the right indicates the range of flux density (Jy beam^{-1}). The ellipse in the bottom-left corner of each panel represents the NOEMA synthesised beam of the 3 mm continuum emission.

1.77×10^5 cm^{-3} for N_2H^+. In the case of N_2H^+ and its isotopologues, we can safely assume LTE as these values for critical density are smaller than the average H_2 volume density of OMC-2 FIR4 (1.2×10^6 cm^{-3}; Ceccarelli et al. 2014b); for $H^{13}CN$ and $HC^{15}N$, the calculated critical density values are the same order of magnitude as the volume density and so the approximation of LTE conditions is reasonable. It should be noted that we used the density value from Ceccarelli et al. (2014b) because it is an average value calculated over the whole system, making it the best comparison that we can make with available data.

Radiative transfer through gas with a constant excitation temperature (T_{ex}) leads to the following expression for the resulting intensity as synthesised beam temperature $T_b(\nu)$:

$$T_b(\nu) = \frac{h\nu}{k}\left(\frac{1}{e^{\frac{h\nu}{kT_{ex}}} - 1} - \frac{1}{e^{\frac{h\nu}{kT_{bg}}} - 1}\right)(1 - e^{-\tau(\nu)}), \quad (2)$$

where c, h and k represent the speed of light, Boltzmann constant and Planck constant, respectively, in cgs units, while $\tau(\nu)$ is the opacity of the line. We take the background temperature (T_{bg}) as that of the cosmic microwave background (CMB; i.e. 2.73 K). The column density N_{TOT} (cm^{-2}) is then obtained directly from the measure of the opacity in the line centre computed in Eq. (2) (τ_0), for which T_b is a maximum:

$$N_{TOT} = \frac{8\pi\nu^3(\Delta v)\tau_0 Q(T_{ex})\sqrt{\pi}}{2\sqrt{ln2}} \frac{e^{\frac{E_u}{kT_{ex}}}}{c^3 A_{ul} g_u (e^{\frac{h\nu}{kT_{ex}}} - 1)}, \quad (3)$$

where ν is frequency (Hz), Δv represents the line width (cm s^{-1}), $Q(T_{ex})$ is the partition function at excitation temperature T_{ex}, E_u is the energy of the upper level (K), A_{ul} is the Einstein coefficient (s^{-1}) and g_u is the upper state degeneracy. Equations (3) and (2), which can be found in the Formalism for the CASSIS software[3] (author: C. Vastel), describe how to compute the total column

[3] http://cassis.irap.omp.eu/docs/RadiativeTransfer.pdf

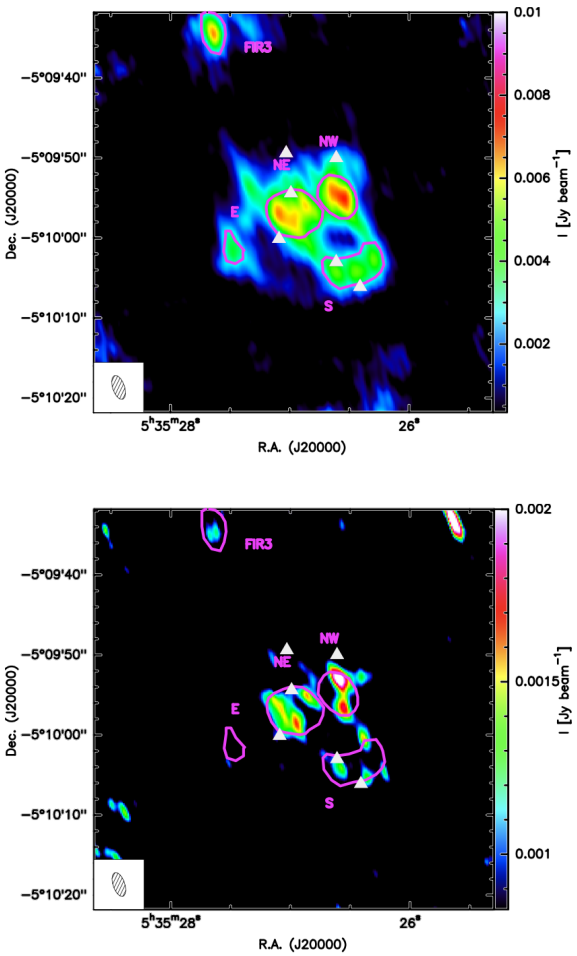

Fig. 4. *Upper panel*: $H^{13}CN$ (1−0) average emission map with extraction regions enclosed by pink curves. *Lower panel*: $HC^{15}N$ (1−0) average emission map with extraction regions enclosed by pink curves. The wedge on the right of each panel indicates the range of flux density (Jy beam^{-1}). The ellipse in the bottom-left corner of each panel represents the NOEMA synthesised beam. White triangles mark the positions of continuum sources as identified by Neri et al. (in prep.).

density (and opacity) from our spectroscopic and observational parameters under the conditions of LTE and optically thin lines. We justify our use of the optically thin assumption in Sects. 4.2 and 4.3 for HCN and N_2H^+, respectively.

4.2. HCN isotopologues

Our analysis obtained opacities ranging from 8.1×10^{-4} to 1.6×10^{-2}, enabling us to assume that the lines are optically thin and use the method described in Sect. 4.1. Due to the fact that we only observed one transition for both $H^{13}CN$ and $HC^{15}N$, the excitation temperature (T_{ex}) cannot be derived directly from the data and it has to be assumed. Therefore, the spectra were modelled for two fixed temperatures, corresponding to the range of temperatures found for FIR4 using previous data: an upper temperature of 45 K and a lower temperature of 35 K (taken from Ceccarelli et al. 2014b; Favre et al. 2018). For FIR3, the upper temperature was fixed at 150 K and the lower temperature was fixed at 100 K (assuming that FIR3 is a hot corino; Tobin et al. 2019; Ceccarelli et al., in prep.). The column density was repeatedly varied until the model matched the observations, taking into account a 10% calibration error in the latter. Using this method, we obtained best-fit values (along with upper and lower limits) for the column densities of $H^{13}CN$ and $HC^{15}N$ in each region. It should be noted that $H^{13}CN$ is potentially better than HCN for computing the $^{14}N/^{15}N$ ratio because HCN is expected to be optically thick. However, the column density ratio $N_{TOT}(H^{13}CN)/N_{TOT}(HC^{15}N)$ has to be corrected by the $^{12}C/^{13}C$ ratio, which was assumed to be 50 ± 5 as measured by Kahane et al. (2018) using CN, HCN and HC_3N lines. The $^{12}C/^{13}C$ ratio measured from HCN specifically in this paper is tentative; the authors calculated their HCN-specific value of 36 ± 15 by comparing $HC^{15}N$ to $H^{13}C^{15}N$. They point out in this paper that due to the weakness (2.5σ) of the $H^{13}C^{15}N$ detection, it is possible that the obtained $^{12}C/^{13}C$ ratio is underestimated (see Kahane et al. 2018 for further discussion). Taking this into account, we decided to use the average value of 50 ± 5. We also note that the uncertainty associated with the average $^{12}C/^{13}C$ ratio calculated in Kahane et al. (2018) is included in our calculated uncertainties associated with $^{14}N/^{15}N$ ratios of HCN.

4.3. N_2H^+

4.3.1. CLASS

Due to the aforementioned presence of HFS, we first used the specific HFS fitting routine that is provided within CLASS to model our spectra. This routine requires the following inputs for each isotopologue: relative intensity, r_i (with sum normalised to 1) and velocity separation from the reference component (computed from the Doppler law based on the frequency differences obtained in the lab), v_i (km s^{-1}) for each HF component. Both inputs were in this case obtained from the Cologne Molecular Database for Spectroscopy (CDMS) for each isotopologue. If we define the central velocity of the ith component as $v_{0,i} = v_i + p_2$, then we can calculate the opacity of our lines, τ, using Eq. (4):

$$\tau(\nu) = p_4 \Sigma_{i=1}^{N} r_i e^{-4\ln 2\left(\frac{\nu - v_i - p_2}{p_3}\right)^2}. \quad (4)$$

In this equation, τ represents the opacity as a function of frequency (ν), N represents the number of HF components, r_i is the relative intensity of the ith HF component and v_i is the velocity separation of the ith HF component from the reference component, (km s^{-1}). The fitting procedure described above provides optically thin lines (see Table 2 for the opacity values obtained by CLASS HFS), and hence we can estimate N_{TOT} from the relation:

$$N_{TOT} = \frac{8\pi W \nu^3}{A_{ul} c^3 g_u} \frac{Q(T_{ex}) e^{\frac{E_u}{kT_{ex}}}}{e^{\frac{h\nu}{kT_{ex}}} - 1} \frac{1}{J_\nu(T_{ex}) - J_\nu(T_{bg})}. \quad (5)$$

Equation (5) provides N_{TOT} from the total integrated intensity of the line (W) in the case of optically thin transitions and all rotational levels being characterised by a single T_{ex}. The equivalent Rayleigh-Jeans temperature, $J_\nu(T)$, is defined as

$$J_\nu(T_{ex,bg}) = \frac{h\nu}{k} \frac{1}{e^{\frac{h\nu}{kT_{ex,bg}}} - 1}. \quad (6)$$

Since we have HFS and optically thin lines, we can calculate the total integrated intensity in two ways: when all HF components are detected, we sum the integrated intensity of all of them; when only the strongest HF component is detected, we multiply its integrated intensity by the known relative ratio with respect to the total.

Table 2. Values for the parameters used in Eqs. (7) and (8), plus those varied during MCMC modelling for N_2H^+ and its ^{15}N isotopologues.

Line	Region	$FWHM$ [km s^{-1}]	V_{LSR} [km s^{-1}]	T_{ex} [K]	Total integrated area [K km s^{-1}]	Opacity
$H^{13}CN$	E region	9.9 ± 3.7	11.4	40 ± 5	4.8 ± 0.5	$(8.2^{+0.7}_{-1.0})$E-03
	NW region	11.73 ± 0.59	11.4	40 ± 5	8.2 ± 0.8	$(1.4^{+0.1}_{-0.1})$E-02
	NE region	12.8 ± 1.2	11.4	40 ± 5	6.2 ± 0.6	$(1.0^{+0.1}_{-0.8})$E-02
	S region	11.34 ± 0.39	11.4	40 ± 5	6.0 ± 0.6	$(1.00^{+0.1}_{-0.1})$E-02
	FIR3	10.6 ± 2.7	11.4	40 ± 5	4.7 ± 0.5	$(6.3^{+0.5}_{-0.7})$E-03
$HC^{15}N$	E region	9.6 ± 3.7	11.4	40 ± 5	0.36 ± 0.04	$(9.0^{+0.5}_{-1.2})$E-04
	NW region	13.20 ± 0.38	11.4	40 ± 5	1.2 ± 0.1	$(2.4^{+0.3}_{-0.3})$E-03
	NE region	12.5 ± 1.2	11.4	40 ± 5	1.2 ± 0.1	$(2.7^{+0.3}_{-0.3})$E-03
	S region	11.74 ± 0.89	11.4	40 ± 5	0.92 ± 0.09	$(2.0^{+0.2}_{-0.2})$E-03
	FIR3	12.85 ± 1.5	11.4	40 ± 5	1.2 ± 0.1	$(2.4^{+0.2}_{-0.2})$E-03
$^{15}NNH^+$	E region	0.80	11.67 [a]	$40.0^{+5.0}_{-5.0}$	0.067 ± 0.007	$(1.2^{+0.2}_{-0.2})$E-03
	NW region	$0.81^{+0.02}_{-0.02}$	$11.31^{+0.07}_{-0.07}$	$40.0^{+0.0}_{-0.0}$	0.14 ± 0.01	0.1± 0.4
	NE region	$0.79^{+0.02}_{-0.02}$	$11.2^{+0.2}_{-0.1}$	$40.0^{+0.4}_{-0.2}$	0.085 ± 0.009	0.1 ± 0.3
	S region	$0.79^{+0.02}_{-0.02}$	$11.5^{+0.2}_{-0.3}$	$39.7^{+0.4}_{-0.4}$	0.13 ± 0.01	0.1 ± 0.9
$N^{15}NH^+$	E region	0.80	10.30 [a]	$40.0^{+5.0}_{-5.0}$	0.10 ± 0.01	$(2.1^{+0.3}_{-0.3})$E-03
	NW region	$0.80^{+0.02}_{-0.02}$	$11.4^{+0.2}_{-0.08}$	$40.0^{+0.2}_{-0.2}$	0.13 ± 0.01	1.4 ± 1.4
	NE region	$0.83^{+0.04}_{-0.07}$	$11.3^{+0.1}_{-0.4}$	$40.4^{+0.6}_{-0.4}$	0.059 ± 0.006	0.1 ± 0.9
	S region	0.80	10.67 [a]	$40.0^{+5.0}_{-5.0}$	0.11 ± 0.01	0.1 ± 0.3
N_2H^+	E region	$0.78^{+0.04}_{-0.04}$	$11.49^{+0.02}_{-0.02}$	$38.6^{+1.0}_{-2.0}$	23 ± 2	3.20 ± 0.08
	NW region	$0.75^{+0.02}_{-0.02}$	$11.11^{+0.02}_{-0.02}$	$38.4^{+2.0}_{-2.0}$	36 ± 4	6.50 ± 0.06
	NE region	$0.97^{+0.02}_{-0.02}$	$11.18^{+0.02}_{-0.02}$	$43.8^{+2.0}_{-6.0}$	30 ± 3	4.95 ± 0.06
	S region	$1.2^{+0.00}_{-0.3}$	$11.2^{+0.3}_{-0.07}$	$37.9^{+7.0}_{-2.0}$	33 ± 3	5.550 ± 0.004

Notes. Calibration errors of 10 and 15% were used in calculations involving the CLASS and MCMC models, respectively. We note that, due to the low spectral resolution, the HFS structure cannot be constrained for HCN isotopologues and so the spectra are fit with one transition only, the FWHM of which is included in this table for each region. Also, for this reason, V_{LSR} is fixed to the accepted source value of 11.4 km s^{-1}. The RMS was 5.1 mK for $H^{13}CN$, 4.4 mK for $HC^{15}N$, 10.1 mK for $^{15}NNH^+$, 10.3 mK for $N^{15}NH^+$ and 31 mK for N_2H^+. [a]Due to low S/N, V_{LSR} is fixed to the value found from a single Gaussian fit of the strongest HF component using L-M fitting.

For the ^{15}N isotopologues, the opacity derived from the fit confirms that we have optically thin lines ($\tau \leq 0.1$) in all but one case: $N^{15}NH^+$ towards the NW region. In this line, the opacity of the sum of the components is ∼1.4, but the error is so large (1.4 ± 1.4) that we can assume optically thin conditions also in this case, following Caselli et al. (2002). For the lines for which only the strongest HF component is detected, we know that this component has a relative intensity of $\frac{5}{9}$ compared to the total; therefore, we divided its integrated intensity by $\frac{5}{9}$ in order to obtain the total integrated intensity, W, for the ^{15}N isotopologues.

On the other hand, the output of the CLASS HFS fitting routine tells us that the opacity of the sum of the components for the main isotopologue (N_2H^+) is larger than 1, meaning that in all cases we have optically thick lines. However, the faintest component, $J'F' - JF = 01 \rightarrow 12$, has, according to the relative intensity ratio, an opacity that is $\frac{3}{27}$ of the total, providing opacities lower than 1 in all spectra. In addition, this component is well separated from the others in the spectrum, therefore its integrated intensity is not contaminated by emission from any other component. We measured its integrated intensity and divided it by the factor $\frac{3}{27}$ to derive the total one.

Table 2 shows the best-fit FWHM and total integrated intensity values of our lines with uncertainties given by:

$$\Delta N_{TOT} = N_{TOT} \frac{\Delta W}{W + 0.1} \quad (7)$$

$$\Delta W = \sqrt{(cal/100 \times W)^2 + (rms \sqrt{2 \times FWHM \times \Delta v_{res}})^2}. \quad (8)$$

In these equations, N_{TOT} and ΔN_{TOT} represent column density (cm^{-2}) and associated error, respectively, W and ΔW represent the integrated area (K cm^{-1}) and associated error, respectively, *cal* represents the calibration error (assumed in this case to be 10%), Δv_{res} represents the velocity resolution (km s^{-1}) (in our case 0.2 km s^{-1}) and rms is 10.1 mK for $^{15}NNH^+$, 10.3 mK for $N^{15}NH^+$ and 31 mK for N_2H^+. From fitting our spectra using L-M fitting in CASSIS, FWHM is obtained as 0.8 km s^{-1}. It should be noted that the values for W obtained using the method

described previously are given in K km s^{-1}; therefore, for Eq. (5), these are converted to K cm s^{-1} as everything else is in cgs units.

All spectroscopic parameters used in Eq. (5) are taken from the CDMS database. The CMB temperature (T_{bg}) is assumed to be 2.73 K. For the excitation temperature (T_{ex}), we cannot constrain this using our analysis alone because, despite resolving the HFS in our spectra, the opacity of the N_2H^+ spectra is not well constrained and the ^{15}N-isotopologue lines are optically thin (see Table 2). Therefore, we must take our values from previous measurements. We fixed T_{ex} to 35 and 45 K (Ceccarelli et al. 2014b; Favre et al. 2018).

4.3.2. CASSIS

Within CASSIS, there is a Python library (LineAnalysisScripting.py) that allows users to create Jython scripts to model sources in LTE using the Markov chain Monte Carlo (MCMC) method. As part of the script, we define a number of parameters that will be varied and give upper and lower limits for the variation range. In most cases, we have sufficient S/Ns to vary four parameters: N_{TOT}, T_{ex}, FWHM and V_{LSR}. From L-M fitting, we know the order of magnitude for N_{TOT} in each case as well as the FWHM for all of the components (~0.8 km s^{-1}). Therefore, N_{TOT} is varied between 10^{10} and 10^{15} cm^{-2} for the ^{15}N isotopologues and between 10^{12} and 10^{15} cm^{-2} for the main isotopologue. From this we also vary FWHM between 0.3 km s^{-1} and 1.2 km s^{-1} in each case. For T_{ex}, once again we use previous research of this source to determine our upper and lower limits: 50 and 30 K, respectively (5 K above and below the upper and lower limits used to model the spectra and calculate N_{TOT} from the CLASS method). Also from previous research, the accepted value for the V_{LSR} of OMC-2 FIR4 is 11.4 km s^{-1} (e.g. Kahane et al. 2018; Ceccarelli et al. 2017); therefore, this parameter is varied between 8 and 15 km s^{-1}.

In the case of the ^{15}N isotopologues, since we have lower S/N in general, we must constrain at least one of the parameters (in cases where we have higher S/N, we obtain good fits by leaving the parameters unfixed and allowing the software to find the best fit; if we have low S/N we cannot do this). Therefore, in these cases, we constrain the range for T_{ex} to just 3σ above and below the T_{ex} value obtained for the main isotopologue in the corresponding position. Meanwhile, three of the spectra show very low S/N: the E Region of both ^{15}N isotopologues as well as the S Region of $N^{15}NH^+$. For these cases, we also constrain the V_{LSR}, fixing this parameter to the value obtained in the corresponding position in the main isotopologue. In all cases, the script is run and the model is compared to the observations.

The values obtained with the two methods are the same within error bars except for the cases with higher opacity (i.e. NW Region) or with low S/N (i.e. E Region in both ^{15}N isotopologues and S Region in $N^{15}NH^+$). For the latter, the fit obtained using MCMC with the aforementioned limits was not optimal and underestimated N_{TOT} with respect to the observations, causing overestimations of the $^{14}N/^{15}N$ ratio. Therefore, we concluded that these three spectra had insufficient S/N to be analysed using MCMC; therefore, to analyse these data, first we fitted a single Gaussian to the strongest HF component using L-M fitting in the relevant spectrum (see Table 2) to obtain a value of V_{LSR} for each spectrum. We used this value to fix V_{LSR} in a line analysis while fixing T_{ex} to 35 and 45 K to give upper and lower limits. The N_{TOT} was then varied manually until good fits were obtained, taking into account a 15% calibration error. The best-fit values in all cases for T_{ex}, FWHM and V_{LSR} are in Table 2. Table 3 shows the column density values for $H^{13}CN$ and $HC^{15}N$ that were obtained from the method described above along with the resultant $^{14}N/^{15}N$ ratios. The resultant values of N_{TOT} for N_2H^+ and its isotopologues (Table 4) were used to calculate the $^{14}N/^{15}N$ ratio for N_2H^+ (Table 5).

Table 3. Values of column density obtained using CASSIS for $H^{13}CN$ and $HC^{15}N$ along with results of analysis using CASSIS for $^{14}N/^{15}N$ in HCN.

Region	N_{TOT} [cm^{-2}]		$^{14}N/^{15}N$
	$H^{13}CN$	$HC^{15}N$	
E region	$(1.9–2.3)\times10^{13}$	$(1.7–2.1)\times10^{12}$	452–676
NW region	$(2.9–4.3)\times10^{13}$	$(5.3–6.5)\times10^{12}$	273–406
NE region	$(2.6–3.2)\times10^{13}$	$(5.4–6.6)\times10^{12}$	197–296
S region	$(2.4–3.0)\times10^{13}$	$(3.9–4.9)\times10^{12}$	245-385
FIR3	$(1.9–2.4)\times10^{13}$	$(5.0–6.3)\times10^{12}$	151–240

Notes. The values were calculated using average values of column densities taken at 35 and 45 K (100 and 150 K for FIR3).

Table 4. Column density values obtained using the two methods (CASSIS HFS and CLASS HFS) for $^{15}NNH^+$, $N^{15}NH^+$ and N_2H^+.

Line	Region	N_{TOT} [cm^{-2}]	
		CASSIS HFS	CLASS HFS
$^{15}NNH^+$	E region	$(3.0^{+0.8}_{-0.7})\times10^{11}$	$(4.3\pm0.6)\times10^{11}$
	NW region	$(5.0^{+0.9}_{-0.9})\times10^{11}$	$(5.3\pm0.7)\times10^{11}$
	NE region	$(3.1^{+0.7}_{-0.7})\times10^{11}$	$(3.8\pm0.5)\times10^{11}$
	S region	$(3.9^{+1.0}_{-1.0})\times10^{11}$	$(4.9\pm0.7)\times10^{11}$
$N^{15}NH^+$	E region	$(4.0^{+1.1}_{-1.0})\times10^{11}$	$(3.7\pm0.3)\times10^{11}$
	NW region	$(4.3^{+1.0}_{-1.0})\times10^{11}$	$(3.8\pm0.6)\times10^{11}$
	NE region	$(2.4^{+0.7}_{-0.9})\times10^{11}$	$(3.6\pm0.5)\times10^{11}$
	S region	$(4.25^{+1.1}_{-1.1})\times10^{11}$	$(6.1\pm0.8)\times10^{11}$
N_2H^+	E region	$(8.2^{+0.6}_{-0.6})\times10^{13}$	$(8.9\pm0.9)\times10^{13}$
	NW region	$(1.21^{+0.09}_{-0.09})\times10^{14}$	$(1.7\pm0.7)\times10^{14}$
	NE region	$(1.1^{+0.1}_{-0.1})\times10^{14}$	$(1.3\pm0.1)\times10^{14}$
	S region	$(1.4^{+0.1}_{-0.2})\times10^{14}$	$(1.6\pm0.2)\times10^{14}$

5. Results

Figure 5 shows a visual comparison between all of the $^{14}N/^{15}N$ ratios obtained during the course of our analysis, while Fig. 6 shows how the $^{14}N/^{15}N$ ratios from our dataset and that described in Fontani et al. (2020) vary across the regions defined in each paper across OMC-2 FIR4. We now explore the results of our analysis of both the HCN and N_2H^+ datasets in detail.

5.1. HCN

As stated above, the column density values for $H^{13}CN$ and $HC^{15}N$ and the calculated $^{14}N/^{15}N$ ratios can be found in Table 3. It is clear from the values that there is an agreement in the $^{14}N/^{15}N$ ratio in the NE, NW and S Regions but a higher value

Table 5. Results of CASSIS HFS and CLASS HFS analysis for $^{14}N/^{15}N$ in N_2H^+.

	CASSIS HFS		CLASS HFS	
Region	$^{14}N/^{15}N$ ($^{15}NNH^+$)	$^{14}N/^{15}N$ ($N^{15}NH^+$)	$^{14}N/^{15}N$ ($^{15}NNH^+$)	$^{14}N/^{15}N$ ($N^{15}NH^+$)
E region (*)	270^{70}_{70}	200^{50}_{50}	200^{40}_{40}	240^{30}_{30}
NW region	240^{20}_{20}	280^{30}_{40}	320^{100}_{100}	450^{200}_{200}
NE region	350^{40}_{40}	460^{70}_{60}	340^{50}_{50}	360^{60}_{60}
S region	350^{60}_{40}	320^{80}_{80}	330^{60}_{60}	260^{50}_{50}

Notes. (*)In the E Region, a different second method was used instead of CLASS HFS due to the HFS structure being invisible (see Sect. 5.2). The values were calculated using average values of column densities taken at 35 and 45 K and can be seen in Table 4.

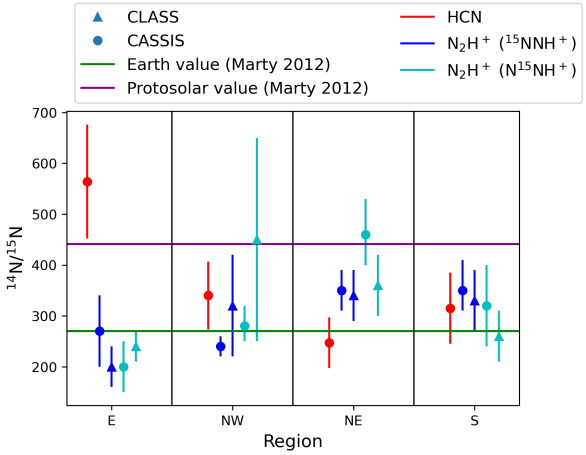

Fig. 5. Visual comparison of the $^{14}N/^{15}N$ ratios obtained for HCN and N_2H^+ in the regions of OMC-2 FIR4, from both CASSIS and CLASS (in the latter case) and as calculated from the different ^{15}N isotopologues (also in the latter case).

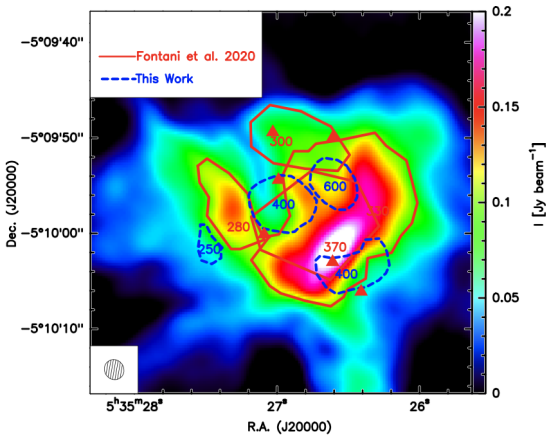

Fig. 6. Combined $^{14}N/^{15}N$ ratios in N_2H^+ in regions defined by Fontani et al. (2020) (red) and in regions defined by our work (blue) overlaid onto N_2H^+ (1–0) emission from Fontani et al. (2020) (colour scale); red triangles show locations of continuum emission sources in FIR4 as identified by Neri et al. (in prep.). The wedge on the right indicates the range of flux density (Jy beam^{-1}). The ellipse in the bottom-left corner represents the ALMA synthesised beam.

is obtained from the E Region. Meanwhile, FIR3 shows the lowest ratio. Overall, these results indicate that no enrichment or depletion in ^{15}N is apparent in the inner sub-regions of FIR4 (i.e. the NW, NE and S Regions) analysed in this work. In fact, the derived $^{14}N/^{15}N$ ratios are consistent with each other (within the uncertainties) as well as with the value obtained at low angular resolution by Kahane et al. (2018): 270 ± 50. The E Region shows the highest $^{14}N/^{15}N$ ratio in HCN; however, it is not straightforward to justify this because, even though the region is the most external one and hence potentially most exposed to external UV photons, a variation due to selective photodissociation would produce a lower $^{14}N/^{15}N$ ratio, which is at odds with our findings.

5.2. N_2H^+

The spectra of N_2H^+ and its ^{15}N isotopologues have been fit according to the methods described in Sect. 4.3.1 and 4.3.2. The resulting values for N_{TOT} and $^{14}N/^{15}N$ ratios are listed in Tables 4 and 5, respectively. The range of $^{14}N/^{15}N$ that we obtain is 200–450.

As one can see, in a similar fashion to the $^{14}N/^{15}N$ ratios obtained from HCN, the ratios that we obtain from N_2H^+ show broad homogeneity across the three central regions. However, while our HCN results show the E Region to have a slightly higher $^{14}N/^{15}N$ ratio, our results for N_2H^+ show the E Region to have a ratio that is still a little lower than most other regions but within error of the ratio found in at least one other region. There is therefore some agreement with previous research (in particular Fontani et al. (2020), who analysed the same N_2H^+ data), which concluded that the $^{14}N/^{15}N$ ratio showed little regional variation across the central regions of FIR4.

There are a few region-specific caveats in our analysis that should be highlighted. We now discuss these in more detail.

Regarding the S Region, as can be clearly seen in Fig. A.1, in most regions the $F_1 = 0-1$ component of N_2H^+ is not blended with the nearby HF components and shows a profile that can be well fitted with a single Gaussian, which also indicates that this particular HF component is likely optically thin, as assumed in Sects. 4.3.1 and 4.3.2. However, in the spectrum of the S Region this component shows two peaks. Interestingly, the $N^{15}NH^+$ line also shows two peaks in its main HF component. In both cases, this profile can be due to two partly overlapping velocity features. The $^{15}NNH^+$ line, instead, shows a single peak in the main component. To probe whether the profile observed in the $F_1 = 0-1$ component of N_2H^+ and in $N^{15}NH^+$ is due to multiple velocity features or self-absorption, we compared the velocities of the two peaks in the $F_1 = 0-1$ component of N_2H^+ (1–0) with those of $N^{15}NH^+$ and $^{15}NNH^+$. In both cases, the velocities of the peak(s) of the emission in the ^{15}N isotopologues coincide with one (or both) of those seen in the isolated component of the N_2H^+ emission. Therefore, we can conclude that the double peak seen both in $N^{15}NH^+$ and in the isolated HF component of N_2H^+ is likely due to two velocity features along the line of sight.

In the NW Region, as stated before, the opacity derived in CLASS that resulted from using the HFS fitting routine is 1.4 ± 1.4. With such a large error associated with a faint line, the opacity cannot be well constrained and this may be causing inaccuracies in our estimates performed assuming optically thin conditions. The slightly larger discrepancy between the ratios obtained using the two analysis methods (CASSIS and CLASS) in the NW Region (see Table 5) can possibly be explained due to these potential inaccuracies.

In the case of the E Region, the line is so faint that only the main component of the HFS is visible in the $^{15}NNH^+$ and $N^{15}NH^+$ spectra. For this reason, the fit to the whole HFS cannot be performed. Therefore, we fitted the main HF component (the only one detected) with a single Gaussian with the resultant brightness temperature (T_b) used to calculate the opacity (τ) using Eq. (2). This opacity was in turn used to calculate the total column density (N_{TOT}) in Eq. (3).

6. Discussion

From our HCN results, we can see that there is a homogeneity in the $^{14}N/^{15}N$ ratio across the central portion of FIR4, from which we extracted the NW, NE and S spectra, but not in the ratio of the E region. The difference in $^{14}N/^{15}N$ ratio between the central three regions and the E region is possibly due to the E region being much further from the centre of FIR4, where conditions affecting ^{15}N production may differ, including any possible outflow influence. A recent paper (Benedettini et al. 2021) found that no nitrogen fractionation was occurring due to the shock in the bow shock of L1157; therefore we cannot and are not confirming that the different result in the E region is definitely due to an external outflow, especially given the lack of evidence. Rather, we are suggesting that this is a potential topic for future research using more sensitive observations.

The ratios obtained from N_2H^+ towards the central part of the source are also largely consistent among them and with those obtained from HCN (as explained previously, it is believed that small discrepancies seen in the results obtained from the two methods are more likely to be due to opacity effects than any true difference in the ratio; see Sect. 5.2). However, in contrast to our HCN results for this region, which show the E Region to vary but not in the way that would be expected if photo-processes were important, our N_2H^+ ratio in the E region shows very little contrast with the ratios of the central regions, being the lowest of the four but still within uncertainty of at least one other region.

Overall, the fact that in both HCN and N_2H^+ isotopologues we find no significant nitrogen fractionation effects confirms the previous findings of Fontani et al. (2020), obtained only for N_2H^+ and analysed in different sub-regions: the nitrogen isotopic ratio in OMC-2 FIR4 in the two most abundant N-bearing species (after N_2) is not influenced significantly at core scales by a local change in physical conditions. In particular, in this work we have investigated for the first time the influence of an enhanced cosmic-ray ionisation rate (see Sect. 5) within the same source and found that this has no effect on the $^{14}N/^{15}N$ ratio, a conclusion that confirms that of Fontani et al. (2020) and also of Benedettini et al. (2021) towards the protostellar bow-shock L1157-B1. The homogeneity that is present particularly across the central regions of FIR4 (NE, NW and S) in both HCN and N_2H^+ also goes towards the current theory that OMC-2 FIR4 is sufficiently embedded that selective photodissociation, which is expected to take place only on the external layers of dense cores exposed to external UV photons, is not present due to the high visual extinction of the source and hence does not affect the fractionation here.

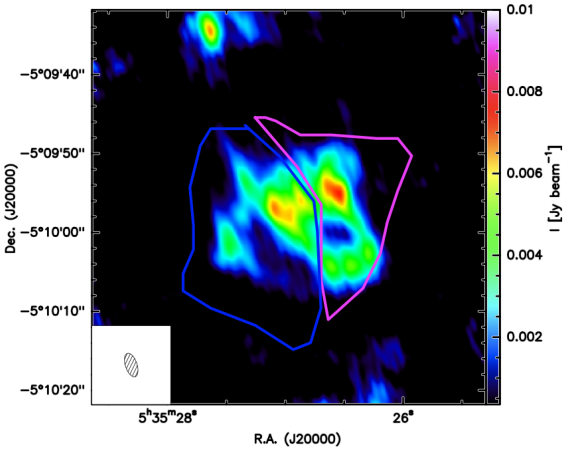

Fig. 7. Average emission map of $H^{13}CN$ (1−0) overlaid with regions defined in Fontani et al. (2017) with suggested higher (blue) and lower (pink) ionisation rate regions. The wedge on the right indicates the range of flux density (Jy beam^{-1}). The ellipse in the bottom-left corner represents the NOEMA synthesised beam.

The absence of significant variations in both species also indicates that selective photodissociation has no effect at the linear scales probed by our observations. Colzi et al. (2019), who studied the high-mass star-forming protocluster IRAS 05358+3543, measured a higher $^{14}N/^{15}N$ ratio in N_2H^+ towards the diffuse region of the protocluster than towards the star-forming cores. Therefore, it was concluded that an enhanced $^{14}N/^{15}N$ ratio in N_2H^+ occurs locally in the diffuse gas of star-forming regions. Despite the larger distance to the source compared to OMC-2 FIR4 (2 kpc vs. 393 pc) and thus the different linear scale, we can compare these results with our own by utilising the fact that the high ionisation rate extraction region (the blue polygon in Fig. 7) overlaps with both the compact E and NE Regions as well as including the more diffuse regions. The consistency in the $^{14}N/^{15}N$ ratio of N_2H^+ between our larger polygon and our more compact NE Region (both ∼400) suggests that, in this region, enrichment due to selective photodissociation caused by external UV photons is not occurring. This result could either be because there is an insufficient external UV field or because the emitting region is too embedded for external UV photons to penetrate and produce this effect. The same 'non-variation' effect appears to be present also in the $^{14}N/^{15}N$ ratios of HCN in OMC-2 FIR4 between the larger, more diffuse extraction region and the more compact NE Region (both ∼250).

7. Conclusions

In this work, within the framework of the Large Program SOLIS, we have mapped the $H^{13}CN$ (1−0) and $HC^{15}N$ (1−0) lines towards the protocluster OMC-2 FIR4 with the NOEMA interferometer. We have also analysed archival data obtained with the ALMA interferometer of the 1–0 lines of N_2H^+ and both its ^{15}N isotopologues. For the first time, we compare at high angular resolution the $^{14}N/^{15}N$ isotopic ratios in HCN and N_2H^+, two important N-bearing species that are expected to possibly behave differently in the enrichment or depletion of ^{15}N. The results can be summarised as follows:

1. $H^{13}CN$ (1−0) and $HC^{15}N$ (1−0) show spatial similarities in their emission, with $H^{13}CN$ showing systematically stronger

emission across all regions of the source. There are obvious peaks to both the $H^{13}CN$ (1−0) and $HC^{15}N$ (1−0) emission in the north-west, north-east and (to a lesser extent in $HC^{15}N$) south of the central area of emission, plus a peak farther to the east in an outer region that appears in $H^{13}CN$ only. A noticeable absence of emission is also present in both species towards the centre of FIR4. There is also a peak in FIR3 in both $H^{13}CN$ (1−0) and $HC^{15}N$ (1−0) emission.

2. The $^{14}N/^{15}N$ ratio in HCN shows consistency across the different regions in which we have decomposed the emission, especially in the central part of FIR4 traced by regions NE, NW and S, while a higher isotopic ratio is found in the E region. This indicates that the main mechanism accepted as being behind enrichments of ^{15}N in HCN (i.e. selective photodissociation) does not seem to play a role in these regions of the protocluster.
3. The $^{14}N/^{15}N$ ratios in N_2H^+ in the same regions as those selected for our HCN analysis are also obtained; these results show agreement with the HCN ratios in that there is consistency across the central regions while in the E region the $^{14}N/^{15}N$ ratio from N_2H^+ slightly varies in the opposite direction compared to the ratio in HCN, although the errors are large. The ratios also show consistency across the central region of FIR4, in agreement with previous findings (Fontani et al. 2020).
4. To further investigate our results, the $^{14}N/^{15}N$ ratio in HCN in regions that have previously shown a different cosmic-ray ionisation rate are analysed and found to be consistent with each other, further cementing our conclusion that the $^{14}N/^{15}N$ ratio is not influenced by local changes in the physical properties across the centre of FIR4.
5. Measuring the $^{14}N/^{15}N$ ratio of N_2H^+ in a region encompassing the diffuse envelope and the E and NE Regions, as well as regions external to both suggests consistency between the diffuse envelope and the NE Region, seemingly confirming a 'non-variation' effect and once again indicating that selective photodissociation seems to be irrelevant in these regions.

It is clear from our results and conclusions that our picture of the evolution of the $^{14}N/^{15}N$ ratio in protostellar environments, as well as on the origin of ^{15}N enrichments in SS small bodies, is still incomplete. More collaboration between theory and observations is needed here in order to resolve these questions. More specifically, in the case of FIR4, the observation of higher transitions will allow us to better constrain parameters such as T_{ex} and N_{TOT} in order to create more accurate models to compare with our observations in both LTE and non-LTE.

Acknowledgements. This project has received funding from (i) the European Union Horizon 2020 research and innovation programme under the Marie Skłodowska-Curie grant agreement No 811312 for the Project "Astro-Chemical Origins", (ACO) and (ii) the European Research Council (ERC) under the European Union Horizon 2020 research and innovation programme, for the Project "The Dawn of Organic Chemistry" (DOC), grant agreement No 741002. This paper makes use of the following ALMA data: ADS/JAO.ALMA#2016.0.00681.S. ALMA is a partnership of ESO (representing its member states), NSF (USA) and NINS (Japan), together with NRC (Canada), MOST and ASIAA (Taiwan) and KASI (Republic of Korea), in cooperation with the Republic of Chile. The Joint ALMA Observatory is operated by ESO, AUI/NRAO and NAOJ. We thank Laura Colzi for useful discussions and are also grateful to the IRAM staff for help with data calibration.

References

Adams, F. C. 2010, ARA&A, 48, 47
Adande, G. R., & Ziurys, L. M. 2012, ApJ, 744, 194
Aléon, J. 2010, ApJ, 722, 1342
Benedettini, M., Viti, S., Codella, C., et al. 2021, A&A, 645, A91
Bizzocchi, L., Caselli, P., Leonardo, E., & Dore, L. 2013, A&A, 555, A109
Bonal, L., Huss, G. R., Krot, A. N., et al. 2010, Geochim. Cosmochim. Acta, 74, 6590
Caselli, P., Walmsley, C. M., Zucconi, A., et al. 2002, ApJ, 565, 344
Ceccarelli, C., Caselli, P., Bockelée-Morvan, D., et al. 2014a, in Protostars and Planets VI, eds. H. Beuther, R. S. Klessen, C. P. Dullemond, & T. Henning (Tucson: University of Arizona Press), 859
Ceccarelli, C., Dominik, C., López-Sepulcre, A., et al. 2014b, ApJ, 790, L1
Ceccarelli, C., Caselli, P., Fontani, F., et al. 2017, ApJ, 850, 176
Chaussidon, M., Robert, F., & McKeegan, K. D. 2006, Geochim. Cosmochim Acta, 70, 5433
Colzi, L., Fontani, F., Caselli, P., et al. 2018a, A&A, 609, A129
Colzi, L., Fontani, F., Rivilla, V. M., et al. 2018b, MNRAS, 478, 3693
Colzi, L., Fontani, F., Caselli, P., et al. 2019, MNRAS, 485, 5543
Daniel, F., Dubernet, M. L., Meuwly, M., Cernicharo, J., & Pagani, L. 2005, MNRAS, 363, 1083
Daniel, F., Gérin, M., Roueff, E., et al. 2013, A&A, 560, A3
Daniel, F., Faure, A., Pagani, L., et al. 2016, A&A, 592, A45
De Simone, M., Fontani, F., Codella, C., et al. 2018, MNRAS, 476, 1982
Endres, C. P., Schlemmer, S., Schilke, P., Stutzki, J., & Müller, H. S. P. 2016, J. Mol. Spectr., 327, 95
Favre, C., Ceccarelli, C., López-Sepulcre, A., et al. 2018, ApJ, 859, 136
Fontani, F., Caselli, P., Palau, A., Bizzocchi, L., & Ceccarelli, C. 2015, ApJ, 808, L46
Fontani, F., Ceccarelli, C., Favre, C., et al. 2017, A&A, 605, A57
Fontani, F., Quaia, G., Ceccarelli, C., et al. 2020, MNRAS, 493, 3412
Fontani, F., Barnes, A. T., Caselli, P., et al. 2021, MNRAS, 503, 4320
Füri, E., & Marty, B. 2015, Nat. Geosci., 8, 515
Furlan, E., Fischer, W. J., Ali, B., et al. 2016, ApJS, 224, 5
Furuya, K., & Aikawa, Y. 2018, ApJ, 857, 105
Gounelle, M., Chaussidon, M., & Rollion-Bard, C. 2013, ApJ, 763, L33
Großschedl, J. E., Alves, J., Meingast, S., et al. 2018, A&A, 619, A106
Guzmán, V. V., Öberg, K. I., Huang, J., Loomis, R., & Qi, C. 2017, ApJ, 836, 30
Hacar, A., Tafalla, M., Forbrich, J., et al. 2018, A&A, 610, A77
Heays, A. N., Visser, R., Gredel, R., et al. 2014, A&A, 562, A61
Hernandez-Vera, M., Kalugina, Y., Denis-Alpizar, O., Stoecklin, T., & Lique, F. c. 2014, J. Chem. Phys., 140, 224302
Hily-Blant, P., Bonal, L., Faure, A., & Quirico, E. 2013, Icarus, 223, 582
Hily-Blant, P., Magalhaes, V., Kastner, J., et al. 2017, A&A, 603, L6
Hily-Blant, P., Pineau des Forêts, G., Faure, A., & Flower, D. R. 2020, A&A, 643, A76
Kahane, C., Jaber Al-Edhari, A., Ceccarelli, C., et al. 2018, ApJ, 852, 130
Kainulainen, J., Stutz, A. M., Stanke, T., et al. 2017, A&A, 600, A141
Lee, S., Nomura, H., Furuya, K., & Lee, J.-E. 2021, ApJ, 908, 82
Lique, F. 2015, MNRAS, 453, 810
Loison, J.-C., Wakelam, V., Gratier, P., & Hickson, K. M. 2019, MNRAS, 484, 2747
López-Sepulcre, A., Taquet, V., Sánchez-Monge, Á., et al. 2013, A&A, 556, A62
Manfroid, J., Jehin, E., Hutsemékers, D., et al. 2009, A&A, 503, 613
Marty, B., Chaussidon, M., Wiens, R. C., Jurewicz, A. J. G., & Burnett, D. S. 2011, Science, 332, 1533
Mumma, M. J., & Charnley, S. B. 2011, ARA&A, 49, 471
Osorio, M., Díaz-Rodríguez, A. K., Anglada, G., et al. 2017, ApJ, 840, 36
Padovani, M., Marcowith, A., Hennebelle, P., & Ferrière, K. 2016, A&A, 590, A8
Redaelli, E., Bizzocchi, L., Caselli, P., et al. 2018, A&A, 617, A7
Rodgers, S. D., & Charnley, S. B. 2008, MNRAS, 385, L48
Romano, D., Matteucci, F., Zhang, Z. Y., Papadopoulos, P. P., & Ivison, R. J. 2017, MNRAS, 470, 401
Romano, D., Matteucci, F., Zhang, Z.-Y., Ivison, R. J., & Ventura, P. 2019, MNRAS, 490, 2838
Roueff, E., Loison, J. C., & Hickson, K. M. 2015, A&A, 576, A99
Shimajiri, Y., Takahashi, S., Takakuwa, S., Saito, M., & Kawabe, R. 2008, ApJ, 683, 255
Shinnaka, Y., Kawakita, H., Kobayashi, H., Nagashima, M., & Boice, D. C. 2014, ApJ, 782, L16
Terzieva, R., & Herbst, E. 2000, MNRAS, 317, 563
Tobin, J. J., Megeath, S. T., van't Hoff, M., et al. 2019, ApJ, 886, 6
Vastel, C., Bottinelli, S., Caux, E., Glorian, J. M., & Boiziot, M. 2015, in SF2A-2015: Proceedings of the Annual meeting of the French Society of Astronomy and Astrophysics, 313
Viti, S., Fontani, F., Jiménez-Serra, I., & Holdship, J. 2019, MNRAS, 486, 4805
Wirström, E. S., & Charnley, S. B. 2018, MNRAS, 474, 3720
Womack, M., Ziurys, L. M., & Wyckoff, S. 1992, ApJ, 387, 417
Zeng, S., Jiménez-Serra, I., Cosentino, G., et al. 2017, A&A, 603, A22

Appendix A: Spectra

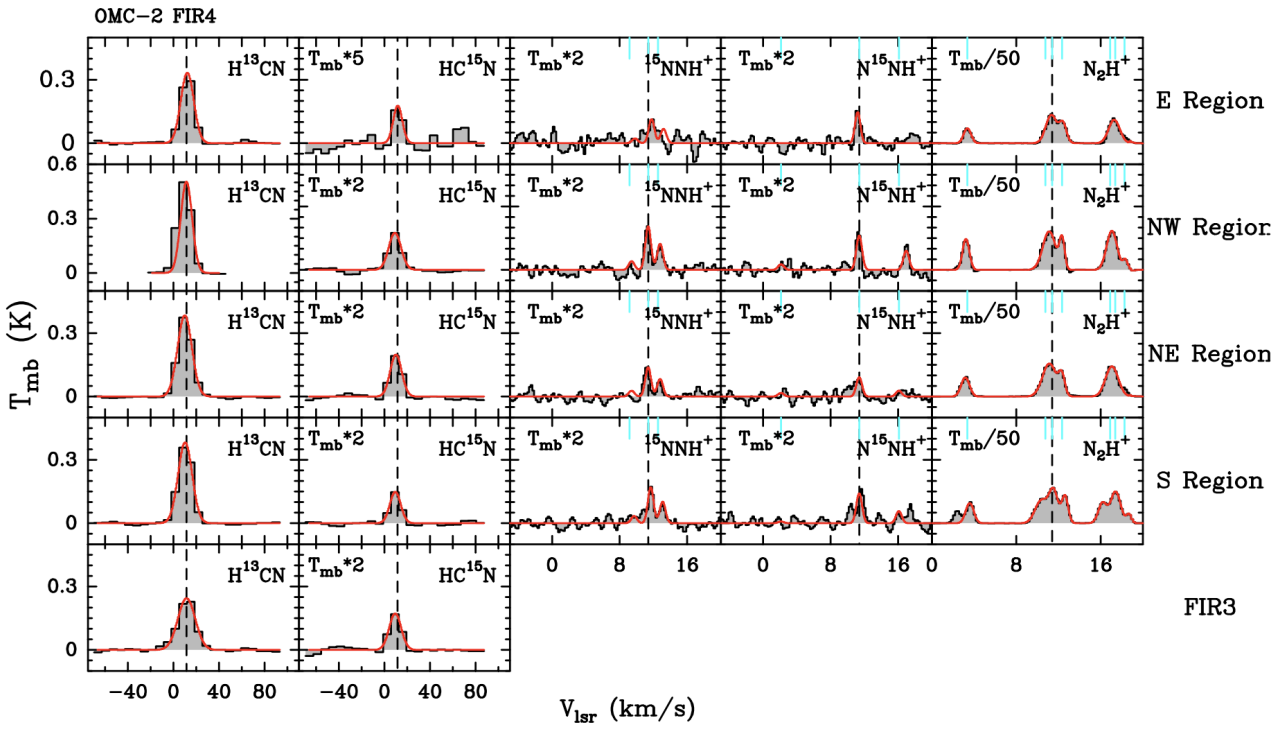

Fig. A.1. Spectra extracted for our study in (left to right) $H^{13}CN$ (1 − 0), $HC^{15}N$ (1 − 0), $^{15}NNH^+$ (1 − 0), $N^{15}NH^+$ (1 − 0) and N_2H^+ (1 − 0); from top to bottom, the spectra extracted in the E, NW, NE, S and FIR3 regions. The CASSIS fits are superimposed in red. The dashed black line represents the V_{LSR} value for this source, which is 11.4 km s^{-1}. The blue lines represent the location of the HFS components for N_2H^+ and its ^{15}N isotopologues.